Opto-Electronic Advances

Article

September 2023, Vol. 6, No. 9

DOI: 10.29026/oea.2023.220154

ITO-free silicon-integrated perovskite electrochemical cell for light-emission and light-detection

Maria Baeva[1,2,3], Dmitry Gets[2], Artem Polushkin[2], Aleksandr Vorobyov[1], Aleksandr Goltaev[1], Vladimir Neplokh[1,4], Alexey Mozharov[1], Dmitry V. Krasnikov[5], Albert G. Nasibulin[5], Ivan Mukhin[1,4]* and Sergey Makarov[2,6]*

Halide perovskite light-emitting electrochemical cells are a novel type of the perovskite optoelectronic devices that differs from the perovskite light-emitting diodes by a simple monolayered architecture. Here, we develop a perovskite electrochemical cell both for light emission and detection, where the active layer consists of a composite material made of halide perovskite microcrystals, polymer support matrix, and added mobile ions. The perovskite electrochemical cell of $CsPbBr_3$:PEO:LiTFSI composition, emitting light at the wavelength of 523 nm, yields the luminance more than 7000 cd/m^2 and electroluminescence efficiency of 1.3×10^5 lm/W. The device fabricated on a silicon substrate with transparent single-walled carbon nanotube film as a top contact exhibits 40% lower Joule heating compared to the perovskite optoelectronic devices fabricated on conventional ITO/glass substrates. Moreover, the device operates as a photodetector with a sensitivity up to 0.75 A/W, specific detectivity of 8.56×10^{11} Jones, and linear dynamic range of 48 dB. The technological potential of such a device is proven by demonstration of 24-pixel indicator display as well as by successful device miniaturization by creation of electroluminescent images with the smallest features less than 50 μm.

Keywords: composite inorganic halide perovskite; silicon; single walled carbon nanotubes; light-emitting electrochemical cell; photodetector; indicator display

Baeva M, Gets D, Polushkin A, Vorobyov A, Goltaev A et al. ITO-free silicon-integrated perovskite electrochemical cell for light-emission and light-detection. *Opto-Electron Adv* **6**, 220154 (2023).

Introduction

The halide perovskites are a family of semiconductor ionic materials possessing unique photoactive, optoelectronic and photonic properties. The first halide perovskite light-emitting diode (PeLED) was demonstrated in the early 90's[1] operating at low temperatures and since then an immense effort has been put into the PeLED devices development[2–8]. Generally, the PeLED architecture

[1]Alferov University, Khlopina 8/3, St. Petersburg 194021, Russia; [2]Department of Physics and Engineering, ITMO University, Lomonosova 9, St. Petersburg 197101, Russia; [3]Institute of Automation and Control Processes (IACP), Far Eastern Branch of Russian Academy of Sciences, Ulitsa Radio 5, Vladivostok 690041, Primorsky Krai, Russia; [4]Peter the Great St. Petersburg Polytechnic University, Polytechnicheskaya 29, St. Petersburg 195251, Russia; [5]Skolkovo Institute of Science and Technology, Nobel 3, Moscow 121205, Russia; [6]Qingdao Innovation and Development Center, Harbin Engineering University, Qingdao 266000, China.

*Correspondence: I Mukhin, E-mail: imukhin@yandex.ru; S Makarov, E-mail: s.makarov@metalab.ifmo.ru

Received: 20 September 2022; Accepted: 27 February 2023; Published online: 26 April 2023

constitutes a complex multilayered structure (see Fig. 1(a)), with strict requirements for intricate material selection and a substantial number of technological steps.

The alternative to PeLEDs in light-emitting devices field of research is perovskite light-emitting electrochemical cells (PeLECs). In contrast to a conventional PeLED multilayered structure, PeLEC consists of a single multifunctional layer[9]—composite perovskite material, i.e., the mixture of inorganic halide perovskite (e.g. $CsPbBr_xCl_{1-x}$) nanocrystals acting as an electroluminescent component embedded into polymer matrix (poly(ethylene oxide) (PEO), poly(ethylene imine) (PEI), etc.), which aids ion transport and passivates crystal grains, and mobile ions (Li^+ from $LiPF_6$, LiTFSI). In such a device, the dynamically formed intrinsic p-i-n structure is responsible for charge injection, facilitation of ion transport, enhanced photoluminescence quantum yield (PLQY) and efficient electroluminescence[10]. To avoid pin-holes formation in the inorganic halide perovskite thin films, a polymer assisted synthesis[11–18] was developed. Already at that, successful light emitting devices were demonstrated, where p-i-n structure was formed by intrinsic ions of composite perovskite material[19,20]. Upon introduction of additional mobile ions, i.e. Li^+, into the polymer/perovskite mix, devices with akin architecture demonstrated lowered threshold voltage, independence on electrode work-function, enhanced current efficiency and electroluminance, and device operation stability improvement[21–24].

In a typical PeLEC structure[19–24] lack of barrier (see Fig. 1(b)) and charge-blocking layers yields poor charge carrier separation and, as a consequence excessive current flowing through the whole device structure, compromising the device operation—there are certain limitations for PeLEC operation regimes. Whereas, a typical PeLED[2–6] involves at least two of the charge-selective transport/barrier layers, as shown in Fig. 1(a), which, while complicating the device fabrication, serves for a purpose of mitigating large currents passing through the structure, improving in-operation stability, compared to PeLEC.

One of the significant issues in PeLEDs and PeLECs application for display design is Joule heating poor endurance of conventional substrates (soda-lime glass, polyethylene terephthalate (PET), etc.)[25–27]. Moreover, indium is depleting element and a key component of transparent conductive oxide (Indium-Tin Oxide, ITO) in the present-day optoelectronics and photovoltaics[28]. Thus, the replacement of ITO by other materials based on earth-abundant elements would aid to prevail the indium deficiency in the industry.

Finally, expanding the functionalities of halogen perovskite devices[29–34] by e.g. combining light-detection (or photovoltaic) regime of operation with light-emitting regime is still an ambitious challenge.

Here we demonstrate PeLEC device consisting of a single layer of composite inorganic perovskite material, i.e. $CsPbBr_3$:PEO:LiTFSI mixture. In contrast to all previously reported advances[10,19,21–24], our device is an ITO-free solution as silicon n-doped substrate was used as bottom electrode, as shown in Fig. 1(b). Owing to the fact that silicon thermal conductivity is substantially higher than that for the ITO/glass structure, our device sustains a much higher level of Joule heating during operation. We also adopt transparent single-walled carbon nanotube (SWCNT) pad as our device top contact[10,19,22,25].

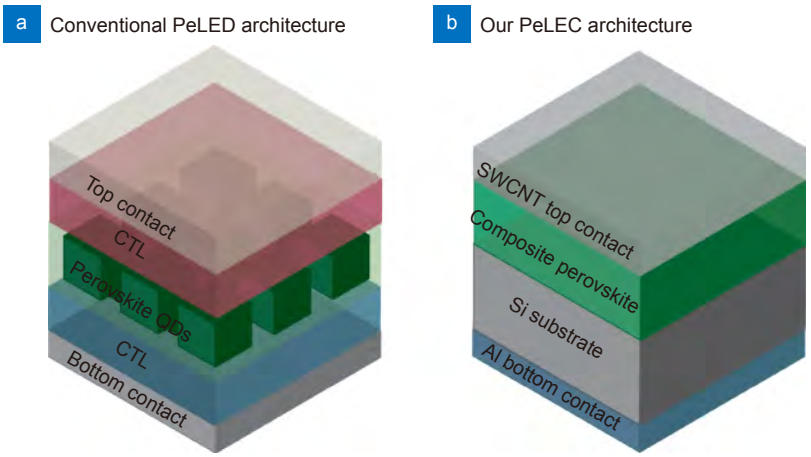

Fig. 1 | Schematic diagrams of (**a**) the typical PeLED device structure, where CTL - charge transfer layer, QD - quantum dots and (**b**) our PeLEC device structure, where SWCNT - single-walled carbon nanotubes.

Our device emits light at bias applied in forward direction and detects light when reversed bias is applied. According to previous developments[36,37] in perovskite devices below a breakdown voltage (U_{BD}) impact ionization occurs. Similarly, evidence revealed in this work suggests that photocurrent elevated growth at $U < U_{ch}$ (certain characteristic bias) is dominated by the avalanche mechanism of charge carrier's emergence.

Moreover, in this work, we discuss the technological potential of perovskite materials integration into the CMOS process by demonstrating the PeLEC/n-Si^{++} indicator display with individual pixels independent addressing and the successful PeLEC device miniaturization. Previously, there were reports of perovskite displays with individual pixels addressing[25,38] and programmable devices[39]. In ref.[25] an 8×8 PeLED display on glass was developed, where $CsPbBr_3$ nanocrystal composite film was enclosed in the conventional multilayer PeLED structure. The operation voltage of such a device was reported to be higher than 8 V, which is much more than the $CsPbBr_3$ bandgap energy. In work[38], the multilayered PeLED display was demonstrated on the Si substrate with enhanced Joule heating endurance and operation voltage > 5 V. Whereas PeLEC devices in our indicator display operate at bias ≥ 3.13 V.

Material and methods

Silicon substrate processing.

We used phosphorous-doped single-crystal silicon substrates <100> (n^{++}-Si(100), $\rho < 0.005$ Ohm·cm) for device fabrication. Firstly, we formed a 200 nm thick silicon dioxide (SiO_2) layer on the surface of the Si substrate via thermal oxidation. Secondly, the substrate was cut into ~2×2 cm samples. Then, a positive photoresist AZ MIR 701 (MicroChemicals GmbH) (film thickness ~ 860 nm) was spin-coated onto the SiO_2/Si side of each sample for photolithography. To fabricate the device area (pixels with 2×2 mm^2 in size), we patterned the photoresist with a laser lithography system Heidelberg Instruments Mikrotechnik DWL 66 FS setup. After that, the photoresist was being developed for 1 minute in AZ 726 MIF developer (MicroChemicals GmbH), washed away afterwards by deionized water and dried with nitrogen flow. Next, we etched away the SiO_2 insulating layer through the patterned photoresist mask with hydrofluoric acid (HF). The residual photoresist was removed using the organic solvent dimethyl sulfoxide (DMSO). The substrate was then washed in deionized water. As a result, an insulating layer of SiO_2 with etched areas was formed on the Si substrate. Finally, bottom aluminum (Al, thickness ~ 200 nm) contact was deposited on the back side of the pre-processed n^{++}-Si(100) substrate by vacuum thermal evaporation in the Boc Edwards Auto 500 set-up at 9×10^{-6} mbar pressure (1 bar=100 kPa). The Si substrate processing scheme is given in Fig. 2(a).

Composite perovskite solution preparation and layer formation

To make perovskite solution of 0.2 molar concentration cesium bromide (CsBr) salt (99.99% purity, Lankhit) was mixed with lead(II) bromide salt (99.99% purity, Lankhit) in a 1∶1 molar ratio, then dissolved in dimethyl sulfoxide (DMSO) (anhydrous DMSO 99.8%, Sigma Aldrich) at 60 °C with overnight stirring at 300 rpm.

For the composite perovskite solution formation the prepared $CsPbBr_3$ DMSO solution, ~1 mol molecular weight (M_V) polyethylene oxide (PEO) (Sigma-Aldrich) DMSO solution (concentration 20 mg·mL^{-1}) and lithium bis(trifluoromethanesulfonyl)imide (LiTFSI) (anhydrous, 99.99% trace metals basis, Sigma-Aldrich) DMSO solution (concentration 10 mg·mL^{-1}) were mixed in 1∶0.1∶0.01 dry components wt. ratio, respectively, with subsequent overnight stirring at 60 °C and 300 rpm.

To prepare the prepatterned n^{++}-Si(100) substrate for composite perovskite layer deposition, its surface was activated in 10 W O_2 plasma (setup model low-cost Zepto, Diener Electronic) for 2 mins to improve wettability to perovskite solution. The composite film (resulting thickness ~ 140 nm, see Fig. 2(b)) was prepared via 80 µL composite solution drop-casting onto the activated sample surface, spinning over 1 min at 1000 rpm, 1 min vacuum treatment at 10^{-3} bar pressure and, lastly, annealing at 60 °C for 5 min. All perovskite solution manipulations were handled in the dry N_2 atmosphere of the MBraun glovebox system.

Transparent top contact formation

Our transparent top contact is based on pads of thin films of single-walled carbon nanotubes (SWCNTs). SWCNTs were produced with an aerosol (floating catalyst) chemical vapor deposition method and collected as a randomly oriented network on nitrocellulose filters (HAWP, Merck Millipore)[40]. We adjusted the collection time to fabricate SWCNT films to reach the transparency of ~80% at 550 nm, which corresponds to the

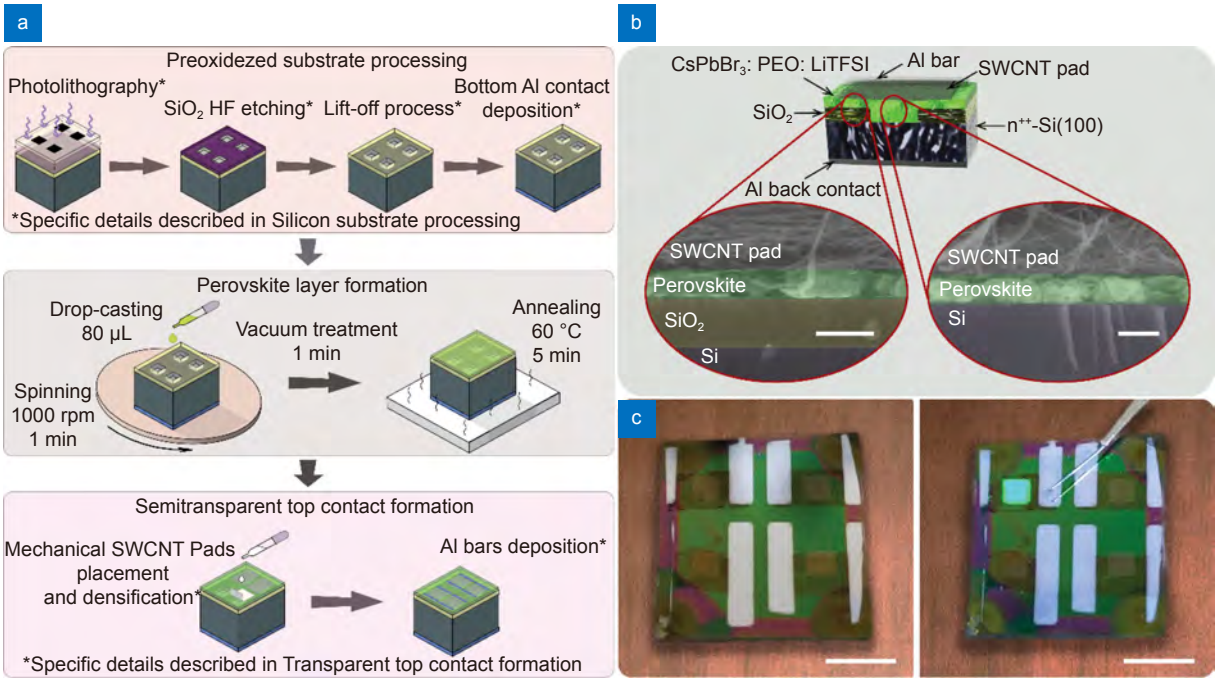

Fig. 2 | (**a**) Dual-function device processing scheme. (**b**) Device cross-section 3D illustration and SEM images, scale bars - 200 nm. (**c**) Final device photos: left panel- without applied bias, right panel- with applied positive bias to one of the pixels, scale bars - 5 mm.

thickness of 23 nm and the sheet resistance of $R_{sh} \geq 100$ Ω/□[41,42]. To form the contacts, SWCNT films were cut with a sharp blade into stripes of 6×4 mm² size and then transferred onto the target substrate surface by means of the dry-transfer technique[43]; anhydrous diisopropyl ether (DIPE) (anhydrous, 99%, contains either BHT or hydroquinone as stabilizer, Sigma Aldtich), preventing underneath perovskite layer dissolving, was used to densify the transferred SWCNT pads, see Fig. 2(a). Lastly, ~60 nm thick Al bars (8.5×1.5 mm²) were deposited on two sides of the active device area directly onto the SWCNT pads by vacuum thermal evaporation method in Vacuum Evaporation Chamber of MBraun glovebox at 3×10^{-6} mbar. The final device photo is presented in Fig. 2(c).

Device SEM imaging

To study the thickness and morphology of the inorganic perovskite layer scanning electron microscopy (SEM) was utilized. For the characterization, the sample was cut across the pixel area. The cross-section (CS) characterization was carried out using Zeiss Supra 25 SEM (accelerating voltage = 5 kV). The CS-SEM images of the structure are given in Fig. 2(b), where the perovskite film thickness constitutes ~140 nm with clearly visible individual perovskite material crystals (grain size ~ 150–200 nm) on the Si substrate.

Device characterization

The device's J-V curves and J tracking curves were acquired with a Keithley 2401 source meter. Data on device electroluminescence and color coordinates were collected with Telescopic Optical Probe 150 of CAS 120 Instrument Systems spectroradiometer. The PeLEC device's radiant power was measured with a Newport 1936-R power meter.

For photodetector behavior measurements, a continuous-wave (CW) laser diode of 450 nm wavelength with the maximum output optical power density of 405.85 mW/cm² (maximum output optical power —6.38 mW; laser spot size 1.57 mm²) was used as an excitation source. The laser output optical power was controlled with an optical filter wheel FW212CNEB, (ThorLabs), that provides a range of illumination intensities. Maximal laser output optical power density equals to ~18 suns in equivalent (eqv.) to AM1,5G spectrum power density at ~450 nm or to ~4 suns in integral (int.) sun power density (also at AM1,5G). The detailed comparison of the experimental laser incident power densities to sun power density, which is important to get a picture on suitability of the device for applications in indoor and outdoor conditions, is shown in SI Table S2. Photodetector external quantum efficiency (EQE) spectra were obtained using a 200 W halide lamp, monochromator Solar Laser Systems M266, and calibrated reference Si

solar cell. The scheme consisting of a modulated light source and lock-in amplifier SRS SR830 was used to subtract the dark signal. A current preamplifier SRS SR570 with a 6 dB band pass filter at the frequency of the modulated light source equal to 571 Hz was connected between the sample and lock-in amplifier. This setup allowed measurements of standard (without applied voltage bias) EQE spectra in the range of 300–1200 nm as well as EQE with bias voltage up to ±5 V.

Heat distribution imaging was acquired with a commercially available IR-imaging camera "Seek Thermal". The two types of samples were compared in this measurement: our n^{++}-Si(100)/$CsPbBr_3$:PEO:LiTFSI/SWCNT structure and the standard soda-lime glass/ITO/$CsPbBr_3$:PEO:LiTFSI/SWCNT structure, both placed on thermo-insulating surface for in-operation imaging. The ITO layer on the glass substrate was patterned by laser ablation (picosecond Nd:YVO_4 laser, series PX100, SOLAR LS) into devices with active area equivalent to structures on n^{++}-Si. All measurements were performed at ambient conditions.

Calculation

The numerical simulation of the dual-function n^{++}-Si(100)/$CsPbBr_3$ heterostructure was performed in the COMSOL Multiphysics package utilizing the drift-diffusion model in 1D geometry across Si/perovskite/SWCNT layers, at the axis normal to the silicon substrate surface. Non-ideality of interfaces of electrical contact layers and the properties of the composite perovskite/SWCNT interface were not taken into consideration. The $CsPbBr_3$ material properties were taken from the literature[11,44–47]. The radiative perovskite recombination rate was estimated with van Roosbroeck-Shockley theory[48]. The Si material parameters were adopted from[49–52], see detailed material parameters in Supplementary information Table S1.

Results and discussion

Figure 2(c) shows our typical final sample design, which consists of four devices (2×2 mm^2 each) with independent transparent SWCNTs pad top contacts and one common aluminum bottom contact. The established device architecture – a single layer of composite perovskite material – $CsPbBr_3$:PEO:LiTFSI – which serves as an active layer in both considered applications: light-emitting electrochemical cell and photodetector, sandwiched in between silicon substrate and SWCNTs pad top electrode.

Light-emitting electrochemical cell performance

The measured composite perovskite PeLEC electroluminescence spectra are shown in Fig. 3(a); the device emits light at the wavelength of 523 nm, which according to the CIE 1931 RGB color space corresponds to the coordinates of x = 0.12 and y = 0.79 (see insert in Fig. 3(b)). This means that the color of our PeLEC device will be able to cover the green color gamut part for the most widely used color gamut standards, such as National Television Standards Committee (NTSC) standard (also see insert in the Fig. 3(a)). The device J-V curve in a combination with its luminance (L) on the applied bias value is shown in Fig. 3(b). The threshold voltage (U_{th}) of the composite perovskite PeLEC is ~3.13 V, which corresponds to $CsPbBr_3$ bandgap energy (~2.4 eV). Slightly higher than expected U_{th} value may be attributed to the significant parasitic series resistance (e.g. due to the over 100 nm active material thickness). From the L-V curve it can be deduced that the maximum achievable luminance of the studied devices is about 7.24 kcd/m^2 at the applied bias of 4.5 V and the current density of 1.15 A/cm^2 (i. e. 10-fold less than in an average analog device[10,19,21–24]). It should be noted, that at the applied bias exceeding 3.5 V a noticeable L-V bent is observed, we speculated that it can be attributed to the device stability issues due to the SWCNT film/perovskite interface phenomena. We built the structure band diagram based on the proposed numerical model (system parasitic series resistance was taken into consideration), see Fig. 3(c). Our device features the II type heterojunction (staggered gap) with the barrier for electrons inside Si substrate. Wherein, due to the silicon substrate high doping concentration, the barrier height is not higher than 35 meV, which practically has almost no influence on the charge carrier injection from Si substrate to perovskite layer when device operates as the light-emitting structure or on charge separation when device operates as photodetector.

The external quantum efficiency of our device was calculated with the following equation:

$$\mathrm{EQE} = \frac{\text{number of photons emitted to the free space per second}}{\text{number of electrons injected into the PeLEC per second}} = \frac{\Phi_e/h\bar{\nu}}{I_F/q},$$

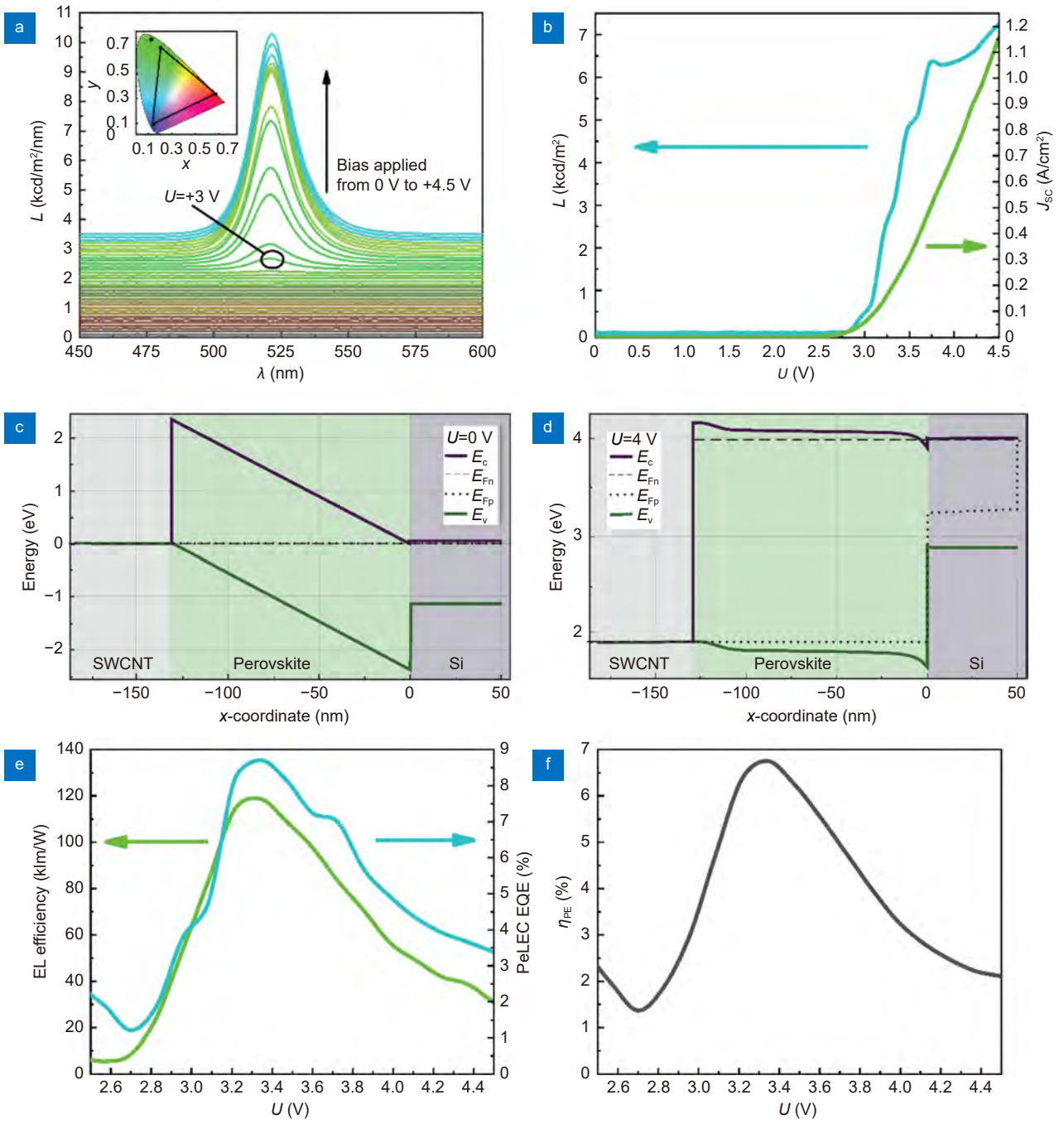

Fig. 3 | Composite perovskite PeLEC key figures-of-merit. (**a**) The device EL spectra on applied bias offset relative to each other, inset – CIE 1931 RGB color space with triangular NTSC color-gamut standard, "star" marker - the device's color coordinates. (**b**) Measured device's J-V curve plot in one axis with L-V curve. (**c, d**) The device's band diagram at 0 V bias (left panel) and 4 V bias (right panel), where E_c and E_v are the perovskite material conduction band bottom and valence band top, respectively, E_{Fn} and E_{Fp} – quasi-Fermi levels for electrons and holes, respectively. (**e**) The device's EL efficiency curve and PeLEC EQE characteristic on applied voltage. (**f**) The device's power efficiency curve.

where Φ_e is PeLECs radiant power, $h\overline{\nu}$ - the energy of a single photon at 523 nm wavelength, I_F - current flowing through the device, q – elemental electron charge. The maximum measured EQE of 8.8% at 3.2 V (see Fig. 3(d)) is in good agreement with the simulation results (see below). A downfall in EQE can be attributed to the enhanced active area degradation process (Cs^+ accelerated migration due, see discussed below) as well as the perovskite active material overheating due to the electrical current flowing directly through the whole structure, not "meeting" obstacles (e.g. charge-selective barriers). The electroluminescence (EL) efficiency curve of our PeLEC

device is given in Fig. 3(d). The maximum EL efficiency of ~120 klm/W is reached at 3.2 V, corresponding to the trend in the EQE curve. The device power efficiency is given by $\eta_{\mathrm{PE}} = \dfrac{\Phi_{\mathrm{e}}}{V_{\mathrm{F}} I_{\mathrm{F}}}$, and reaches ~6.9% at 3.3 V, see Fig. 3(e) (comparable to the aforementioned analogues).

In Fig. 4(a), we present the simulated PeLEC's J-V curves for two different charge carrier lifetimes. From both of these cases it is clear that there is a substantial fraction of current density attributed to the direct charge carriers passing through the entire perovskite layer (note the difference between "Total current" and "Total inelastic current" in the Fig. 4(a), both left and right panels), which seems to be the main PeLECs device performance constraint. The fraction of current density associated with radiative recombination is directly dependent on non-radiative rate, which is characterized by the charge carrier's lifetime. According to our simulation results, the light-emitting device internal quantum efficiency (IQE) exhibits an acute rise when the diode opens followed by only a slight change with higher applied bias, see Fig. 4(b). From the curve in Fig. 4(c), it is clear that IQE changes from 10% to 75% when the charge carrier's lifetime increases from 5 ns to 120 ns. In order to analyze the reported values of EQE we studied light direction extraction emitted by the perovskite layer. We determined the maximum extraction efficiency of ~ 13%. From the emitted light electric field vector modulus map, see SI Fig. S1(b), angular distribution similar to isotropic is observed. In such cases, the average extraction efficiency constitutes 9.2%. Hence, the experimentally observed data can be explained by the assumption that most of PeLEC's light emission gets absorbed by the Si substrate, consequently, an optical perovskite/Si interface optimization becomes a prospect.

To dynamically investigate the PeLEC performance, the current density and luminance tracking was performed at a constant applied bias of 3.7 V during 8 minutes, the data are shown in Fig. 5(a). Before bias applying (Fig. 5(c) panel No. Ⅰ) the perovskite active region consists of uniformly distributed "mixture" of positively charged Li^+ ions (come from Li salt) with no intrinsic bias. The initial current density growth from $t = 0$ sec to t~240 s (see Fig. 5(c) panel No. Ⅱ) is associated with charge redistribution through Li^+ ions migration

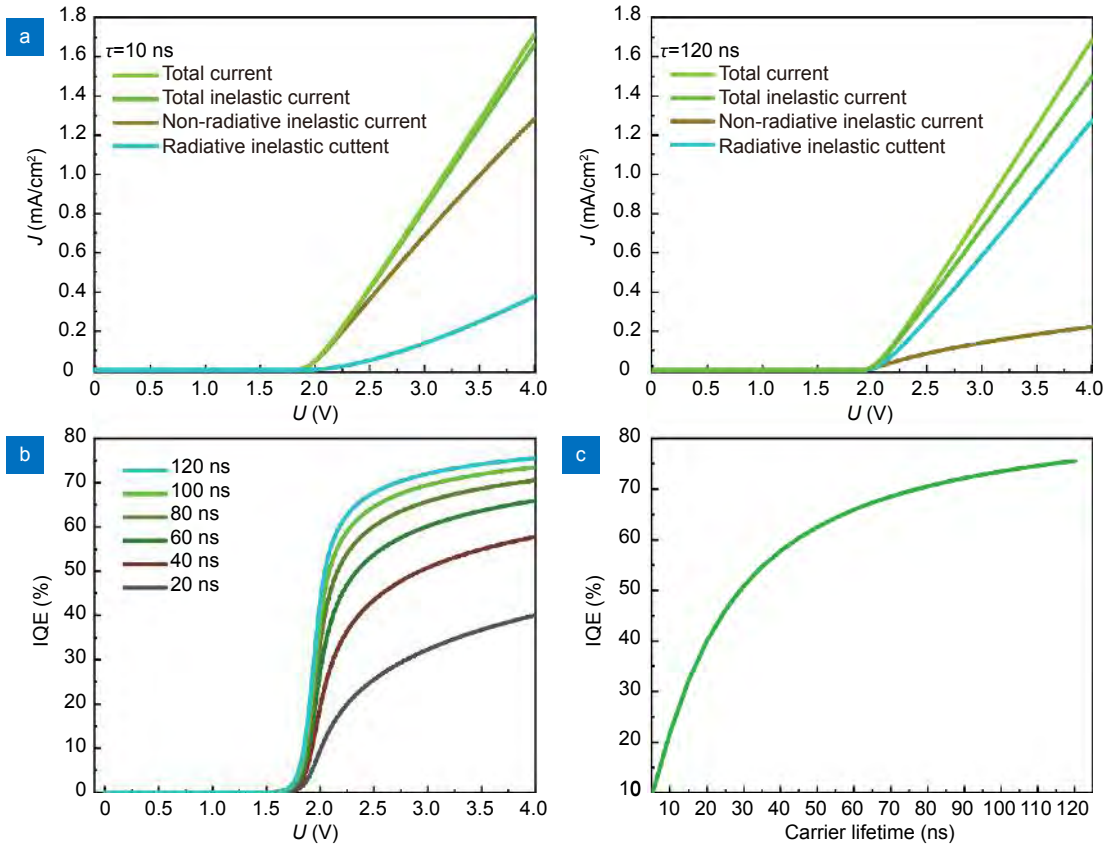

Fig. 4 | (**a**) The PeLEC J-V curves at positive applied bias for charge carrier lifetimes: τ = 10 ns (left panel) and τ = 120 ns (right panel). (**b**) The PeLECs IQE at different charge carriers' lifetimes versus applied bias. (**c**) Combined IQE curve versus charge carrier lifetime at 4 V.

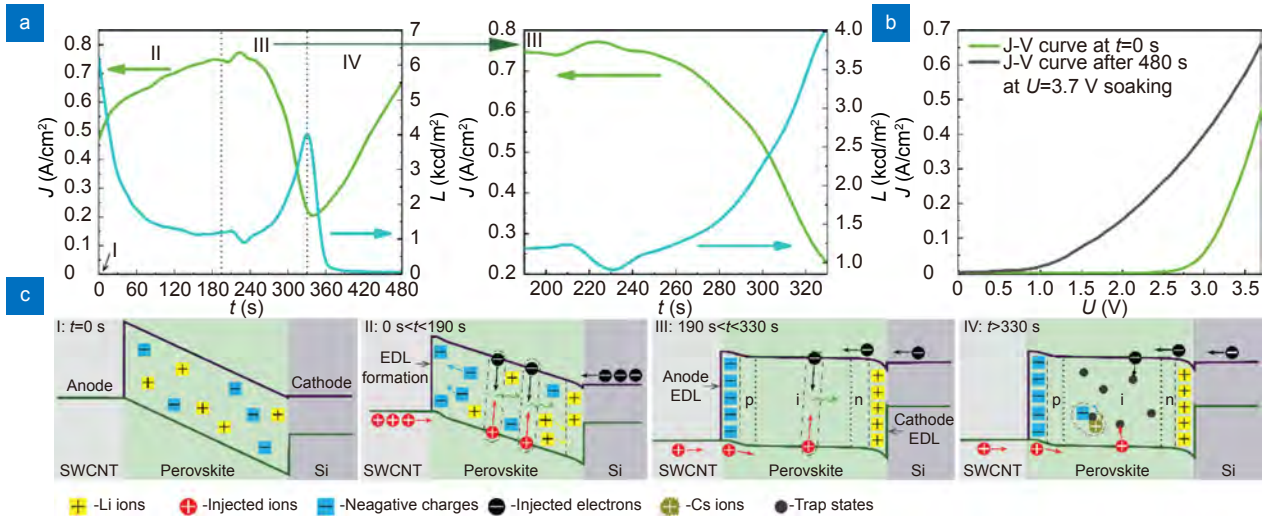

Fig. 5 | (**a**) Left panel – PeLECs J and L tracking over 8 minutes at 3.7 V, right panel – zoomed in maximum current density point in the J curve. (**b**) Comparison of the J-V curves before and after soaking. (**c**) Schematic simplified PeLEC' energy level diagram combined with underlying ionic movement scenario.

with simultaneous electrical double layers (EDLs) formation. At approximately 240 s point in time the p-i-n structure, over the whole 140 nm perovskite thin film thickness, is completely formed – with the lowest conductivity inside of the composite perovskite intrinsic region, hence a "dip" in luminance is observed as well (see Fig. 5(c) panel No. Ⅲ). After the 240 s mark the device enters a semi-stable operation regime with a steady radiative recombination rate, that can be deducted from growth in L curve. From 330 s (see Fig. 5(c) panel No. Ⅳ) due to the high enough applied bias voltage migration of the bigger Cs^+ starts to play a major role in device operation, slowly disrupting the active material microstructure increasing non-radiative recombination inside of the device and leading to final drop in PeLEC luminance. In Fig. 5(b) the comparison of PeLEC's J-V curve before and after voltage soaking is presented: after soaking curve substantiates the ion migration active material degradation with U_{th} being only around 1 V.

All presented in this report device in-operation characterization was carried out during the first 72 h after fabrication. Our devices' lifetime under operation at 2.6 V (luminance 300 cd/m^2) was measured to be 4800 s (~1 h and 20 min) before inevitable active layer degradation (short-cut observed). Nevertheless, composite perovskite PeLECs demonstrate distinctive on-shelf stability—they retain their light-emitting properties (with the similar EL efficiency) over 1440 h (more than two months). We believe that PeLEC on-shelf lifetime significantly exceeds two months, although we did not check much further.

Technological potential demonstrations

To illustrate the applicability of our PeLEC devices, we designed and fabricated an indicator display frame, in a form of printed circuit board (PCB), for six samples, having total of 24 n^{++}-Si(100)/$CsPbBr_3$:PEO:LiTFSI/SWCNT pad pixels, with possibility to address every individual pixel separately using a separate addressing pixels PCB, see Fig. 6(a). As can be seen from the images in the Fig. 6(b–m), that even though all samples were processed manually, a good conformity among all samples is achievable, allowing all pixels to exert distinct light-emitting properties, assigning a good potential to further technological development in n^{++}-Si(100)/$CsPbBr_3$:PEO:LiTFSI/SWCNT pad devices scalability route.

We demonstrated not only the fully operational display based on our device, but also, we took a chance to creatively demonstrate the miniaturization potential of our PeLEC structures, see Fig. 7. To synthesize devices shown in the Fig. 7, the same, as described in *Material and methods* section, n^{++}-Si(100) substrate patterning process was performed, but the different set of patterns, depicting an inverted cat, Alferov University and ITMO University emblems, was used. The consequent fabrication was identical to the "standard" square device manufacturing route. We show that the smallest device's distinguishable details, especially in Fig. 7(b), can reach well beyond 50 μm, which proves the possibility of using our technology for high-density small-area pixel display applications (microdisplays).

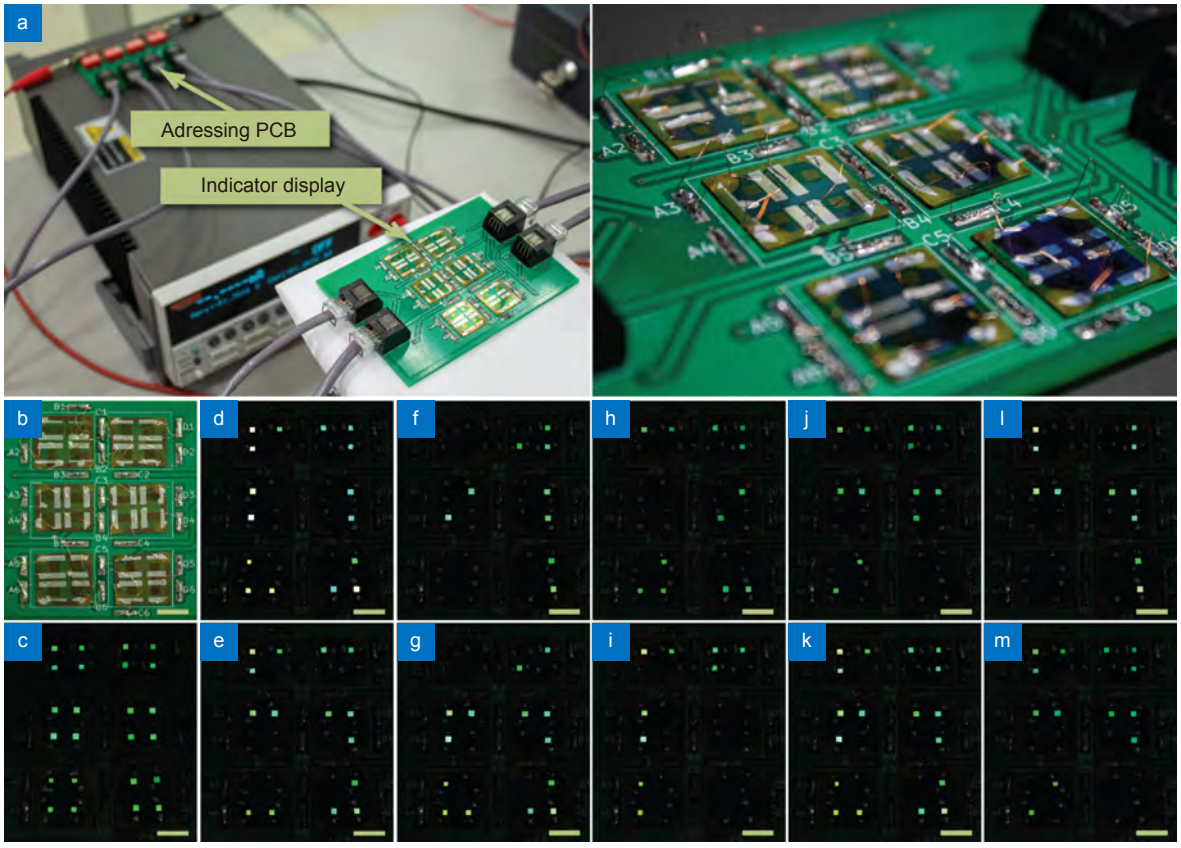

Fig. 6 | The dual-function PeLEC devices indicator display images. (**a**) The entire indicator displays frame PCB and addressing pixels PCB (left panel) with zoomed-in image of the mounted onto the indicator display frame devices (right panel). (**b**) Day-light indicator display image. (**c**) Low ambient light all-pixels-in-operation indicator display image. (**d-m**) Numbers from 0 to 9 images displayed with our indicator display. Scale bars in all images – 1 cm.

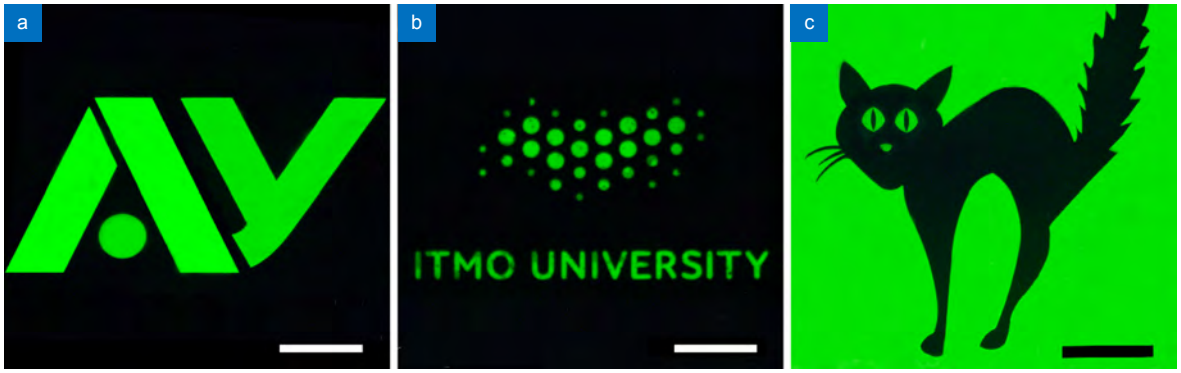

Fig. 7 | Optical images of our n^{++}-Si(100)/$CsPbBr_3$:PEO:LiTFSI/SWCNT mat devices in shape of. (**a**) Alferov University (Saint-Petersburg, Russia) emblem. (**b**) ITMO University (Saint-Petersburg, Russia) emblem. (**c**) Inverted composite perovskite cat. Scale bars in all images are 500 μm.

Light-detecting performance

To evaluate light-detecting device performance, we measured devices J-V curves in dark and under laser illumination, as well as its external quantum efficiency (EQE) and responsivity (R).

The typical J-V curves for the device operating in the regime of photodetector are shown in Fig. 8(a). When the applied to the cell bias exceeds a certain critical voltage — U_{ch} ("characteristic bias") — there is an apparent current growth, which is evidently different from the current curves' shape when the applied bias is above U_{ch}. We introduce the arbitral parameter U_{ch} purely for convenience purposes, although, in terms of underlying physical sense U_{ch} is defined as avalanche photodiode breakdown voltage (fit details on that can be found in Supplementary information Section 4)[53,54]. Moreover,

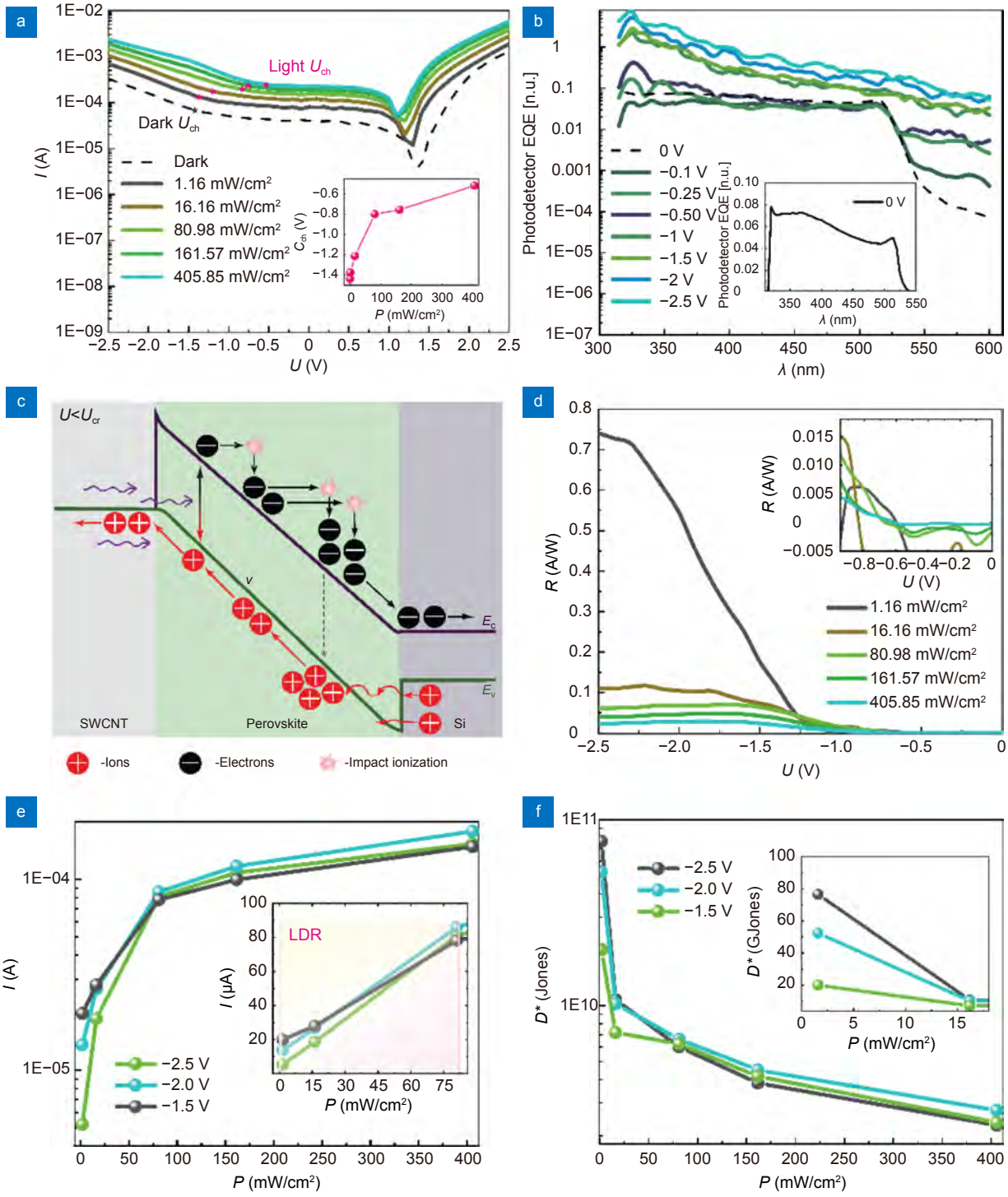

Fig. 8 | Composite perovskite photodiode key figures-of-merit. (**a**) J-V curves at different laser incident radiant power densities, insert – U_{ch} values on incident radiant power density. (**b**) Photodetector EQE on the electrical bias, insert – the device's EQE at U = 0 V in linear axis. (**c**) Schematic simplified PeLEC' energy level diagram in light-detecting operation regime. (**d**) The device's responsivity for different laser incident radiant power densities, insert – zoomed-in section of the graph from U = 0 V to U_{ch} . (**e**) The device's LDR curves for three different biases, insert – LDR region for three biases in linear axis. (**f**) The device's specific detectivity curves for different laser incident radiant power densities, insert – zoomed-in section of the graph for maximal D^* in linear axis.

U_{ch} inversely depends on the incident radiant power density—from −1.25 V at dark to −0.75 V at maximum incident radiant power density. Dependence of U_{ch} on the incident radiant power density is shown in insert from the Fig. 8(a).

The photodetector EQE spectral study provides details

on the system operation regime at negative applied bias, see Fig. 8(b). At −0.5 V < U < 0 in the longer wavelength spectral range (550 nm < λ < 600 nm), the EQE curves' position raises, with respect to each other, is presumably associated with the leakage currents from the Si substrate through the perovskite photoactive layer as well as the low selectivity of the electrodes. Moreover, there is almost no prominent difference between EQE curves for −0.5 V < U < 0 in the shorter wavelength spectral range (corresponding to light absorption in perovskite layer[52]). The further the negative applied bias is lowered, the more conspicuous the EQE curves' position raise, with respect to each other, becomes in full spectral range (300 nm < λ < 600 nm), with the highest values being present in the UV region, which is associated with the enhanced light absorption at the SWCNT/perovskite interface.

The device responsivity—a measure of photodetector's sensitivity to light, expressed as $R = \frac{I_{\rm ph}}{W_{\rm opt}}$, where $I_{\rm ph}$ – photocurrent passing through the device, and $W_{\rm opt}$ – incident radiation power. In Fig. 8(d) for $U_{\rm ch}$ < U < 0 various incident power densities R curves behave akin fluctuating around 0 and their behavior reflects the photodetector linear operational regime—the regime where one absorbed in the perovskite layer photon generates one electron-hole pair, which separates in combined built-in and applied electrical fields and transfers to the respective contact layers – at smaller negative bias. When the applied bias goes below $U_{\rm ch}$, we observe an increase in responsivity for all incident power densities (see Fig. 8(d)). That R increase is the steepest for the minimal incident power density. To note—the minimal incident radial power density in Fig. 8(d) is comparable to incident radial power density (at λ = 450 nm) used in EQE measurements, hence, for $\lambda \le$ 350 nm at U < −1 V, in particular, the EQE is higher than 100%, which seems an evidence of nonlinear operation regime.

In Fig. 8(c), we illustrated the perovskite device band diagram bending in the light-detecting operation regime. To interpret the light-detection at λ < 523 nm, we compared the ideal maximal responsivity (which would correspond to 100% EQE at −2.5 V) in linear operational regime, $R_{\rm id}$ = 0.36 A/W, to the observed maximal responsivity, R = 0.75 A/W. This conveys that the maximal possible light-to-charge conversion current in a linear operational regime has been exceeded, therefore the device operates in the nonlinear regime. When U goes below −1 V the corresponding electric field inside of the perovskite layer reaches values around 10^5 V/cm, which coincides with the typical for effective impact ionization electric field values for some semiconductors[55,56]. We assume that the impact ionization mechanism is responsible for the nonlinear operational regime of our device. Although there are very few previous reports on impact ionization in perovskite materials[36,37]. We suggest that the photocurrent amplification mechanism goes as follows: a high energy photon (UV photon) after its absorption in perovskite generates an electron-hole pair with high kinetic energy close to the SWCNT/perovskite interface. The generated charge carrier pair separates and both charges drift to their corresponding perovskite layer interfaces encountering the electric field induced acceleration, which consequently leads to the charge carriers' kinetic energy growth. Close proximity of the generated electron-hole pare to the SWCNT/perovskite interface increases the effective path of electrons to the cathode. This, in turn, leads to extra increasing the kinetic energy of drifted field-accelerated electrons, which becomes enough for impact ionization and generation of excess carriers (i.e. photocurrent amplification). Comparing the charge carrier mobilities for $CsPbBr_3$ material, see Supplementary information Table S1, as well as taking into consideration the light absorption occurring predominantly near the SWCNT/perovskite interface, we are able to state, that electrons with a much higher probability, than holes, can gain the high kinetic energy, sufficient to launch avalanche mechanism in the photodetector structure.

In Fig. 8(b), EQE spectral dependence curves grow with decreasing wavelength—we attribute that to an increase in the average excess kinetic energy transferred from a photon to an electron, as well as to an increase in the spectral absorption coefficient and a shift of the average depth of light penetration closer to the SWCNT/perovskite interface. That growth correlates with the lowest incident radial power density curve steep growth in Fig. 8(d), although, in itself is not able to describe the more gradual R curves growth for higher incident radial power densities. It is imperative to mention, that the electric field induced charge carrier acceleration is kinetic in nature and the associated energy losses in the material structure are unavoidable, e.g. charge carriers phonon scattering. This conclusion also supports the previously mentioned fact that used in the experiment incident radiant power densities are comparable to the sun's (AM1,5G spectrum) radiant power density. Such high

incident radiant power densities unavoidably lead to the diode structure thermal heating, and, as a consequence, photon scattering induced losses increase. In conventional semiconductors the charge carrier mobility follows $\mu\ T^{-3/2}$ equation, where μ – charge carrier mobility [cm²/V/s], T – temperature [K], which limits the charge carrier electric field induced drifting velocity ($v = \mu \times E$) and kinetic energy ($W_k\ v^2$) leading to the decrease in impact ionization probability and, subsequently, the R values.

To further give necessary evaluation to our photodetector performance, an evaluation of key figures-of-merit were executed. We evaluated the linear dynamic range (LDR) of our photodetector. By definition, the device's LDR illustrates the range of laser optical powers where the detected signal (photocurrent) is linearly proportional to the laser incident radiant power. The LDR is calculated as $R_{\mathrm{LD}} = 20 \times \log\left(\frac{W_{\max}}{W_{\min}}\right)$, where $W_{\max}$ and $W_{\min}$ are maximum and minimum applied laser incident radiant powers providing linear signal response. The dependences of photocurrent from the applied laser power at three applied voltages: −2.5 V, −2 V and −1.5 V are presented in the Fig. 8(e), where the device LDR is marked in the insert graph, giving us LDR equal to 48 dB in the range from 25.38×10^{-3} mW to 1.2 mW applied laser powers.

Next, we looked at specific detectivity (D^*)—a crucial photodetector figure-of-merit, that helps to assess the photodetectors signal-to-noise ratio – is normally approximates as $D^* = R/\sqrt{2qJ_{\mathrm{dark}}}$, where R is the device responsivity at a given bias and laser incident radiant power [A/W], q – elemental electron charge and J_{dark} – corresponding dark current density. Our photodiode's curves for three characteristic biases: −2.5 V, −2 V and −1.5 V, depending on the laser incident radiant power are given in Fig. 8(f). The device's highest specific detectivity value reached 7.65×10^{10} Jones at −2.5 V bias and 25.38×10^{-3} mW laser incident radiant power.

All in all, we conclude that even though the PeLEC demonstrates an impactful potential for light-detection, there are indisputable flaws in the architecture of our device. Further optimization of charge separation layers and electrode selectivity is required.

Heat distribution study

To evaluate in-operation temperature dissipation in our dual-function device on Si substrate compared to temperature dissipation in conventional soda-lime glass/ITO substrate structures infra-red (IR) imaging was utilized. The two identical in device area (active region thickness and material), transparent top contact processing, but different in the substrate material devices were prepared. One sample had n⁺⁺-Si(100)/Al as its bottom contact, while another one had ITO/glass. The typical in-operation images of two types of devices are shown in Supplementary information Fig. S3(a) and S3(b), respectively. For the device on ITO/soda-lime glass the consumed power was equal to 139.3 mW at applied 3.5 V (ITO based device does not endure $V > 3.5$ V, shunting at higher biases) and 0.0398 A current (device $T = 33$ °C), as for n⁺⁺-Si(100)/Al device 207.0 mW of electrical power was consumed at 4.5 V and 0.046 A current (device $T = 24$ °C). Hence, our device on n⁺⁺-Si(100)/Al substrate withstands 32.7% higher applied power with 40% lower thermal heating, compared to the ITO/glass-based device.

In our numerical calculations, the system on Si substrate emits 2.5 times more heat than the system on glass. The numerically simulated maps to compare two studied systems are given in Supplementary information Fig. S3(c) and S3(d). Despite the elevated, compared to the soda-lime glass case, heat dissipation in the active region for the Si substrate case, silicon provides an effective "heat-withdrawal" route from the active perovskite region, which becomes crucial for large area light-emitting devices applications, such as displays.

Conclusion

We have demonstrated the dual-function light-emitting/light-detecting perovskite device on a silicon substrate proving its high technological potential by not only fabrication of an indicator display with individual pixel addressing, but also, we have achieved high resolution with our miniaturized devices. Our light emitting device is a light-emitting electrochemical cell, which provides light electroluminescence efficiency of 1.3×10^5 lm/W and luminance more than 7000 cd/m². In the light-detecting regime of operation, sensitivity of our device reaches 0.75 A/W with specific detectivity 8.56×10^{11} Jones and LDR 48 dB. We have successfully shown that silicon is a promising substrate for applications where devices are required to withstand high thermal heating (i.e. 40% lower thermal heating, when 32.7% higher electrical power is applied). Although, we admit there are optimization prospects to our technology as well, such as optical interface engineering between Si

and perovskite layer (e.g. Al layer for "mirror"-like surface) and device electrical stability improvement via transport and/or passivation layers introduction (e.g. amorphous GaP or GaN layer would act as a hole-blocking layer).

References

1. Era M, Morimoto S, Tsutsui T, Saito S. Organic-inorganic heterostructure electroluminescent device using a layered perovskite semiconductor $(C_6H_5C_2H_4NH_3)_2PbI_4$. *Appl Phys Lett* **65**, 676–678 (1994).
2. Veldhuis SA, Boix PP, Yantara N, Li MJ, Sum TC et al. Perovskite materials for light-emitting diodes and lasers. *Adv Mater* **28**, 6804–6834 (2016).
3. Shan QS, Song JZ, Zou YS, Li JH, Xu LM et al. High performance metal halide perovskite light-emitting diode: from material design to device optimization. *Small* **13**, 1701770 (2017).
4. Jia P, Lu M, Sun SQ, Gao YB, Wang R et al. Recent advances in flexible perovskite light-emitting diodes. *Adv Mater Interfaces* **8**, 2100441 (2021).
5. Liu XK, Xu WD, Bai S, Jin YZ, Wang JP et al. Metal halide perovskites for light-emitting diodes. *Nat Mater* **20**, 10–21 (2021).
6. Lu M, Zhang Y, Wang SX, Guo J, Yu WW et al. Metal halide perovskite light-emitting devices: promising technology for next-generation displays. *Adv Funct Mater* **29**, 1902008 (2019).
7. Li ZT, Cao K, Li JS, Tang Y, Ding XR et al. Review of blue perovskite light emitting diodes with optimization strategies for perovskite film and device structure. *Opto-Electron Adv* **4**, 200019 (2021).
8. Elbanna A, Chaykun K, Lekina Y, Liu YD, Febriansyah B et al. Perovskite-transition metal dichalcogenides heterostructures: recent advances and future perspectives. *Opto-Electron Sci* **1**, 220006 (2022).
9. Youssef K, Li Y, O'Keeffe S, Li L, Pei QB. Fundamentals of materials selection for light-emitting electrochemical cells. *Adv Funct Mater* **30**, 1909102 (2020).
10. Gets D, Alahbakhshi M, Mishra A, Haroldson R, Papadimitratos A et al. Reconfigurable perovskite LEC: effects of ionic additives and dual function devices. *Adv Opt Mater* **9**, 2001715 (2021).
11. Ling YC, Tian Y, Wang X, Wang JC, Knox JM et al. Enhanced optical and electrical properties of polymer-assisted all-inorganic perovskites for light-emitting diodes. *Adv Mater* **28**, 8983–8989 (2016).
12. Chang S, Bai ZL, Zhong HZ. In situ fabricated perovskite nanocrystals: a revolution in optical materials. *Adv Opt Mater* **6**, 1800380 (2018).
13. Xu TF, Meng Y, Wang MS, Li MX, Ahmadi M et al. Poly(ethylene oxide)-assisted energy funneling for efficient perovskite light emission. *J Mater Chem C* **7**, 8287–8293 (2019).
14. Cai WQ, Chen ZM, Li ZC, Yan L, Zhang DL et al. Polymer-assisted in situ growth of all-inorganic perovskite nanocrystal film for efficient and stable pure-red light-emitting devices. *ACS Appl Mater Interfaces* **10**, 42564–42572 (2018).
15. Sakthi Velu K, Anandha Raj J, Sathappan P, Suganya Bharathi B, Mohan Doss S et al. Poly (ethylene glycol) stabilized synthesis of inorganic cesium lead iodide polycrystalline light-absorber for perovskite solar cell. *Mater Lett* **240**, 132–135 (2019).
16. Kim DH, Kim YC, An HJ, Myoung JM. Enhanced brightness of red light-emitting diodes based on $CsPbBr_xI_{3-x}$-PEOXA composite films. *J Alloys Compd* **845**, 156272 (2020).
17. Bansode U, Rahman A, Ogale S. Low-temperature processing of optimally polymer-wrapped α-$CsPbI_3$ for self-powered flexible photo-detector application. *J Mater Chem C* **7**, 6986–6996 (2019).
18. Wang KH, Wang L, Liu YY, Song YH, Yin YC et al. High quality $CsPbI_{3-x}Br_x$ thin films enabled by synergetic regulation of fluorine polymers and amino acid molecules for efficient pure red light emitting diodes. *Adv Opt Mater* **9**, 2001684 (2021).
19. Ishteev A, Haroldson R, Gets D, Tsapenko A, Alahbakhshi M et al. Ambipolar perovskite light electrochemical cell for transparent display devices. arXiv: 1911.06875, 2019. https://doi.org/10.48550/arXiv.1911.06875
20. Miroshnichenko AS, Deriabin KV, Baeva M, Kochetkov FM, Neplokh V et al. Flexible perovskite $CsPbBr_3$ light emitting devices integrated with GaP nanowire arrays in highly transparent and durable functionalized silicones. *J Phys Chem Lett* **12**, 9672–9676 (2021).
21. Alahbakhshi M, Mishra A, Haroldson R, Ishteev A, Moon J et al. Bright and efficient perovskite light emitting electrochemical cells leveraging ionic additives. arXiv: 1909.03318, 2019. https://doi.org/10.48550/arXiv.1909.03318
22. Alahbakhshi M, Papadimitratos A, Haroldson R, Mishra A, Ishteev A et al. Bright perovskite light-emitting electrochemical cell utilizing CNT sheets as a tunable charge injector. *Proc SPIE* **11473**, 114731N (2020).
23. Mishra A, Alahbakhshi M, Haroldson R, Gu Q, Zakhidov AA et al. Pure blue electroluminescence by differentiated ion motion in a single layer perovskite device. *Adv Funct Mater* **31**, 2102006 (2021).
24. Mishra A, Alahbakhshi M, Haroldson R, Bastatas LD, Gu Q et al. Enhanced operational stability of perovskite light-emitting electrochemical cells leveraging ionic additives. *Adv Opt Mater* **8**, 2000226 (2020).
25. Tien CH, Yeh NP, Lee KL, Chen LC. Achieving matrix quantum dot light-emitting display based on all-inorganic $CsPbBr_3$ perovskite nanocrystal composites. *IEEE Access* **9**, 128919–128924 (2021).
26. Teng PP, Reichert S, Xu WD, Yang SC, Fu F et al. Degradation and self-repairing in perovskite light-emitting diodes. *Matter* **4**, 3710–3724 (2021).
27. Bowring AR, Bertoluzzi L, O'Regan BC, McGehee MD. Reverse bias behavior of halide perovskite solar cells. *Adv Energy Mater* **8**, 1702365 (2018).
28. Lokanc M, Eggert R, Redlinger M. The availability of indium: the present, medium term, and long term. Golden: National Renewable Energy Laboratory, 2015.
29. Xie JS, Hang PJ, Wang H, Zhao SH, Li G et al. Perovskite bifunctional device with improved electroluminescent and photovoltaic performance through interfacial energy-band engineering. *Adv Mater* **31**, 1902543 (2019).
30. Shan QS, Wei CT, Jiang Y, Song JZ, Zou YS et al. Perovskite light-emitting/detecting bifunctional fibres for wearable LiFi communication. *Light Sci Appl* **9**, 163 (2020).
31. Shin DH, Shin SH, Choi SH. Self-powered and flexible perovskite photodiode/solar cell bifunctional devices with MoS_2 hole transport layer. *Appl Surf Sci* **514**, 145880 (2020).
32. Liu ZD, Duan CH, Liu F, Chan CCS, Zhu HP et al. Perovskite bi-

functional diode with high photovoltaic and electroluminescent performance by holistic defect passivation. *Small* **18**, 2105196 (2022).
33. Yang SZ, Guo ZL, Gao LG, Yu FY, Zhang C et al. Bifunctional dye molecule in all-inorganic $CsPbIBr_2$ perovskite solar cells with efficiency exceeding 10%. *Sol RRL* **3**, 1900212 (2019).
34. Li XL, Long KC, Zhang G, Zou WT, Jiang SQ et al. Lead-free perovskite-based bifunctional device for both photoelectric conversion and energy storage. *ACS Appl Energy Mater* **4**, 7952–7958 (2021).
35. Marunchenko AA, Baranov MA, Ushakova EV, Ryabov DR, Pushkarev AP et al. Single-walled carbon nanotube thin film for flexible and highly responsive perovskite photodetector. *Adv Funct Mater* **32**, 2109834 (2022).
36. Manousakis E. Optimizing the role of impact ionization in conventional insulators. *Sci Rep* **9**, 20395 (2019).
37. Xu ZH, Yu YG, Niaz IA, Chen UM, Arya S et al. Discovery of ionic impact ionization (I3) in perovskites triggered by a single photon. arXiv: 1906.02475, 2019. https://doi.org/10.48550/arXiv.1906.02475
38. Xu H, Wang XC, Li Y, Cai L, Tan YS et al. Prominent heat dissipation in perovskite light-emitting diodes with reduced efficiency droop for silicon-based display. *J Phys Chem Lett* **11**, 3689–3698 (2020).
39. Zhou NJ, Bekenstein Y, Eisler CN, Zhang DD, Schwartzberg AM et al. Perovskite nanowire-block copolymer composites with digitally programmable polarization anisotropy. *Sci Adv* **5**, eaav8141 (2019).
40. Khabushev EM, Krasnikov DV, Zaremba OT, Tsapenko AP, Goldt AE et al. Machine learning for tailoring optoelectronic properties of single-walled carbon nanotube films. *J Phys Chem Lett* **10**, 6962–6966 (2019).
41. Anoshkin IV, Nasibulin AG, Tian Y, Liu BL, Jiang H et al. Hybrid carbon source for single-walled carbon nanotube synthesis by aerosol CVD method. *Carbon* **78**, 130–136 (2014).
42. Tsapenko AP, Goldt AE, Shulga E, Popov ZI, Maslakov KI et al. Highly conductive and transparent films of $HAuCl_4$-doped single-walled carbon nanotubes for flexible applications. *Carbon* **130**, 448–457 (2018).
43. Kaskela A, Nasibulin AG, Timmermans MY, Aitchison B, Papadimitratos A et al. Aerosol-synthesized SWCNT networks with tunable conductivity and transparency by a dry transfer technique. *Nano Lett* **10**, 4349–4355 (2010).
44. Tao SX, Schmidt I, Brocks G, Jiang JK, Tranca I et al. Absolute energy level positions in tin- and lead-based halide perovskites. *Nat Commun* **10**, 2560 (2019).
45. Saidaminov MI, Haque MA, Almutlaq J, Sarmah S, Miao XH et al. Inorganic lead halide perovskite single crystals: phase-selective low-temperature growth, carrier transport properties, and self-powered photodetection. *Adv Opt Mater* **5**, 1600704 (2017).
46. Yang Z, Surrente A, Galkowski K, Miyata A, Portugall O et al. Impact of the halide cage on the electronic properties of fully inorganic cesium lead halide perovskites. *ACS Energy Lett* **2**, 1621–1627 (2017).
47. Akkerman QA, Motti SG, Srimath Kandada AR, Mosconi E, D'innocenzo V et al. Solution synthesis approach to colloidal cesium lead halide perovskite nanoplatelets with monolayer-level thickness control. *J Am Chem Soc* **138**, 1010–1016 (2016).
48. Varshni YP. Band-to-band radiative recombination in groups IV, VI, and III-V semiconductors (I). *Phys Status Solidi (B)* **19**, 459–514 (1967).
49. Adachi S. *Properties of Group-IV, III-V and II-VI Semiconductors* (John Wiley & Sons, Ltd. , Hoboken, 2005).
50. Jacoboni C, Canali C, Ottaviani G, Quaranta AA. A review of some charge transport properties of silicon. *Solid State Electron* **20**, 77–89 (1977).
51. del Alamo JA, Swanson RM. Modelling of minority-carrier transport in heavily doped silicon emitters. *Solid State Electron* **30**, 1127–1136 (1987).
52. Tyagi MS, Van Overstraeten R. Minority carrier recombination in heavily-doped silicon. *Solid State Electron* **26**, 577–597 (1983).
53. Piprek J. *Semiconductor Optoelectronic Devices: Introduction to Physics and Simulation* (Academic Press, San Diego, 2003).
54. Sze SM, Li YM, Ng KK. *Physics of Semiconductor Devices* (John Wiley & Sons, Ltd. , New York, 2021).
55. Atourki L, Vega E, Mollar M, Marí B, Kirou H et al. Impact of iodide substitution on the physical properties and stability of cesium lead halide perovskite thin films $CsPbBr_{3-x}I_x$ ($0 \le x \le 1$). *J Alloys Compd* **702**, 404–409 (2017).
56. Mikhailova A, Rogachev MP. Impact ionization and Auger recombination in InAs. *Sov Phys Semicond* **10**, 866–871 (1976).

Acknowledgements

M. Baeva, A. Vorobyov, V. Neplokh acknowledge the Russian Science Foundation No. 22-79-10286 (https://rscf.ru/project/22-79-10286/) for supporting silicon substrate processing. D. Gets, A. Polushkin and S. Makarov acknowledge the Ministry of Science and Higher Education of the Russian Federation (Project 075-15-2021-589) for supporting perovskite synthesis. A. G. Nasibulin and D. V. Krasnikov acknowledge the Russian Science Foundation (grant No. 20-73-10256) for supporting synthesis of SWCNTs. We also thank Dr. E. Danilovskiy for valuable engineering advice and N. Zverkov for technical assistance.

Competing interests

The authors declare no competing financial interests.

Supplementary information

Supplementary information for this paper is available at https://doi.org/10.29026/oea.2023.220154